Homogeneous ⟷ Inhomogenous Surface Geometry Transitions Induced by Adsorbed Surfactants in Water/Vapor Interfaces

Nitesh Kumar[a*] and Aurora E Clark[a,b*]

[a] *Department of Chemistry, University of Utah, Salt Lake City, UT, 84112*
[b] *Pacific Northwest National Laboratory, Richland, Washington 99354, United States.*
[*]E-mail: nitesh.kumar@utah.edu, aurora.clark@utah.edu
(Dated: March 6, 2024)

As described by capillary wave theory, adsorbates at a water/vapor interface change surface geometry and fluctuations through altered surface tension. Detailed theoretical studies of surface geometry in the presence of adsorbates, specifically amphiphilic surfactants are relatively sparse and many applications have focused upon ensemble average surface geometric characteristics. In this work we demonstrate that different interpretations of surface geometry emerge when considering the distributions of the geometric descriptors of surface curvature and orientation as a function of adsorbed surfactant concentration and sterics. Molecular dynamics simulations of tributyl phosphate (TBP) adsorbed to the water/vapor surface indicate that increased surface coverage homogeneously enhances symmetric sharp surface waves until a critical concentration is reached that is concomitant with TBP self-assembly. Thereafter, the convexity and concavity of the surface stop cancelling one another and skewing of the surface geometry metric distributions is increased. We define this as a homogeneous → inhomogenous surface geometry transition. Examining the surface geometry as a function of alkyl chain length reveals that smaller surfactants at surface coverages below that needed for surfactant-surfactant interactions *inhomogenously* enhance surface curvature on the surface and that adsorbed alkyl tails to the surface can stabilize and increase homogeneous distributed surface geometric metrics. We label this an inhomogenous → homogeneous geometric transition. These results reflect the opportunity to incorporate more realistic distributions of surface geometry within the collective understanding of capillary wave theory and the relationship between surface geometry and macroscopic properties like surface tension.

Keywords: Molecular Adsorption, Capillary Wave Fluctuations, Surface Curvature, Instantaneous Surface.

Liquid/liquid and liquid/vapor interfaces catalyze numerous biological and chemical reactions.[1, 2] Their temporal dynamics, including but not limited to capillary waves create unique topographical features (crests and troughs) with different chemical properties.[3–6] The qualitative changes to surface dynamics and structure have been noted for various surfactants and can be influenced by factors such as surfactant concentration, headgroup polarity, or hydrophobic chain length.[7–10]

Within capillary wave theory (CWT) the Hamiltonian represents the work done to change the surface area from an ideal plane to the capillary wave surface. Different formulations can be written in terms of surface waves or interfacial characteristics. Perhaps the simplest definition is the free energy of deformation (ΔG_{def}) equivalent to the change in the surface area (ΔA) multiplied by the surface tension γ in Eqn.1: [11, 12]

$$\Delta G_{def} \approx \gamma * \Delta A. \tag{1}$$

In the original work of Stillinger,[13] only liquid/vapor interfaces were considered, however extensions that account for the coupling of the two surfaces that form the liquid/liquid interface were later performed by Ladanyi and coworkers.[14] That work noted that a more complete description of the surface Hamiltonian was needed to account for curvature effects, for example those induced by surfactants. Based upon prior work of the impact of surfactant upon interfacial organization, there is no doubt that surfactants impact capillary wave structure and, through Eqn. 1, the interfacial tension and width.[7, 15, 16]

Understanding surfactant effects upon surface geometry is in its nascent stages. Systems with similar macroscopic properties $(\Delta A$ or $\gamma)$ may have very different topographical characteristics. Additionally, the structural features of the surfactant can have surprisingly large effects upon surface deformation and tension. Consider sodium(alkyl)benzene-sulfonates surfactants, where increasing the alkyl tail length from $10 \longrightarrow 12$ leads to an ≈ 250 % decrease in surface tension at low surfactant concentrations.[17] While significant efforts have been made toward understanding the geometrical properties of surfaces (e.g. curvature and interfacial width) and integrating these factors into CWT, a more comprehensive understanding of surfactant effects remains lacking.[18–22] In this work, the concentration dependent changes to the water/vapor surface geometry and CWT fluctua-

tions are examined for a representative surfactant, tributyl phosphate (TBP) and a systematic series where the length of the alkyl chains are decreased. We compare and contrast the ensemble average and distributions of geometric measures like surface curvature and orientation. The aim is to understand the sensitivity of surface geometry distributions to surfactant concentration and structure; relationships with surface fluctuations are explored.

System Configurations. Initial system configurations (Table S1) were generated using Packmol,[23] and consisted of a central water box with two vapor interfaces containing adsorbed surfactant (Figure 1). Each rectangular box had dimensions of $60 \times 60 \times 180$ Å in the x, y, and z directions, respectively. The TBP concentration was increased from 0 (pure water/vapor) to 240 TBP by increments of 24 TBP. The total number of H_2O was 7205. To understand the effect of the hydrophobic chain length on the surface curvature, simulations with tripropylphosphate (TPP), triethylphosphate (TEP) and trimethylphosphate (TMP) were performed, where 96 surfactant molecules were added randomly to the two water/vapor surfaces (48 per interface). Total surface coverages are provided in Table I.

Molecular Dynamics Simulations. All-atom molecular dynamics (MD) simulations were performed using GROMACS.[24] Molecular motions were integrated with the Leapfrog motion integrator and a 2 fs timestep at 298 K. Each system was first energy-minimized using the steepest descent algorithm for 50,000 timesteps, followed by a 40 ns simulation in the NVT ensemble, where the last 20 ns of data were used for analyses. The system temperature was maintained constant using the Nose-Hoover thermostat with a 0.1 ps temperature coupling time.[25] Long-range interactions were treated using the particle mesh Ewald summation (PME), and short-range non-bonded interactions were calculated with a cutoff of 16 Å. Hydrogen-containing bonds were constrained using the LINCS algorithm.[26] Water was described with the TIP3P model,[27] while the GAFF parameters optimized by Ye et al. were used for TBP.[28] The remaining alkyl-phosphate molecules were modeled using the standard General Amber Force Field (GAFF) force fields without additional optimization.[29] Lennard-Jones cross terms were computed using the Lorentz-Berthelot combination rules.

Definition of the Instantaneous Surface. The Willard-Chandler [30, 31] (WC) surface is continuous coarse-grained representation of the discrete instantaneous water surface configurations, performed by implementing normalized Gaussian density fields at the molecular position of instantaneous water (O-atoms), **r**:

$$\phi(\mathbf{r}, \xi) = (2\pi\xi^2)^{\frac{-D}{2}} \, exp\left(\frac{-r^2}{2\xi^2}\right). \tag{2}$$

Here, ξ represents the coarse grain length, and D is the dimension of the box. The density field is interpolated on a spatial grid that covers the simulation cell. The Marching-cube algorithm (MCA),[32] as implemented in the Pytim package[33] is used to obtain the WC surface. MCA scans the density within each grid and generates vertices and triangulated faces based on the presence of density within the cubic grids. We adopt the suggested coarse grain length criterion of 2.5 Å and 90% bulk density to obtain the instantaneous surface of the water. The resulting WC representation is shown as the solid blue surface in Figure 1.

The sensitivity of ΔA and the geometric properties of the surface as a function of coarse grained length are presented in Figure S1. The interfacial areas are averaged over both surfaces in the simulation box and the ΔA is time-averaged over the entire simulation trajectory, comprising M snapshots:

$$\langle \Delta A \rangle = \frac{1}{M} \sum_{j=1}^{M} A(\rho'(r, j)) - A, \tag{3}$$

where $A(\rho'(r, j))$ is the instantaneous surface area (averaged over both surfaces) at snapshot j, and A is the flat surface area xy Å^2. To calculate the free energy of deformation (Eqn. 1), the surface tension is obtained using the pressure tensor method as an integral over the box length L_z.[34]

Geometric and Temporal Measures of Surface Deformation. The interfacial width d is a measure of the surface deformation in the z-dimension over the entire simulation trajectory and is obtained by fitting the distribution of water density along z using the function[35]:

$$\rho_w(z) = \frac{1}{2}\rho_w - \frac{1}{2}\rho_w \, \text{erf}\left(\frac{z - z_{0,w}}{\sqrt{2}\,d}\right). \tag{4}$$

Here, erf is the error function, ρ_w is the bulk water density, and $z_{0,w}$ is the average position of the interface.

Surface roughness (S_r) is analogous to d and uses the discretized surface representation via the height h in z of the i vertices within the triangulated mesh:

$$\overline{S}_r = \sqrt{\frac{1}{N} \sum_i \delta h_i^2(z)}. \tag{5}$$

Here, $\delta h_i(z) = h_i(z) - \langle h_i(z) \rangle$ represents the difference in the height of the ith vertex from the average height, and
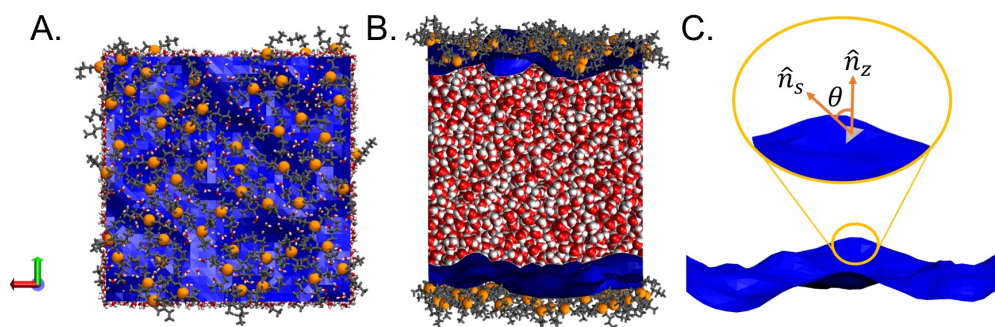
FIG. 1: Schematic of (A) vertical and (B) horizontal views of the simulated water/vapor system laden with TBP (tributyl phosphate). The instantaneous Willard-Chandler (WC) surface is shown in blue. (C) Illustration of the surface orientation angle obtained from the triangulated WC surface.

N represents the total number of vertices in the surface mesh.[36] $\overline{S}_r$ is averaged over both surfaces in the system and presented as a distribution over the entire simulation trajectory.

Measures of Surface Geometry. Surface curvature characterizes the degree to which the surface deviates from an ideal plane. In 2-d, the curvature is the inverse of the radius of curvature, $\kappa_2 = 1/r$. Extending this to 3-d, the curvature at each q_i vertex in the triangulated mesh is defined by two principal curvatures, $\kappa_1(q_i)$ and $\kappa_2(q_i)$. These are employed to define the mean and Gaussian curvature. The mean curvature at any point, denoted as $\kappa_m(q_i) = (\kappa_1(q_i) + \kappa_2(q_i))/2$ is then averaged over all vertices on the surface to define $\overline{\kappa}_m$ which measures the average surface bending. A value of $\overline{\kappa}_m < 0$ or > 0 represents concave and convex surfaces, respectively, while $\overline{\kappa}_m = 0$ represents cancellation of any convexity and concavity to yield a flat average surface.

Gaussian curvature is the product of the two mean principal curvatures ($\overline{\kappa}_1$ and $\overline{\kappa}_2$), as ($\overline{\kappa}_G = \overline{\kappa}_1 * \overline{\kappa}_2$) and reflects the surface topography. For instance, in a torus, the convex region has a positive $\overline{\kappa}_G$ and the inner concave region has a negative value. We further defined the shape descriptor, curvedness $\kappa_C^2(q_i)$,[37] at each vertex in the triangulated mesh using the two principal curvatures as

$$\kappa_C^2(q_i) = \kappa_1^2(q_i) + \kappa_2^2(q_i), \quad (6)$$

where the average surface curvedness for the instantaneous surface is

$$\overline{\kappa_C^2} = \frac{1}{N}\sum_{i=1}^{N}\kappa_C^2(q_i), \quad (7)$$

over the N vertices. Importantly, curvedness describes the total magnitude of surface curvedness irrespective of

positive or negative principle curvature. Thus, higher values of $\overline{\kappa_C^2}$ in the case of a liquid/liquid surface indicate higher surface deformation.[37, 38] $\overline{\kappa_C^2}$ is presented both as a distribution over the whole trajectory, as well as an averaged over all snapshots in the trajectory as $\langle\overline{\kappa_C^2}\rangle$.

Surface orientation is an additional measure of the geometry and is calculated by taking the dot product of the surface normal $\hat{n}_s$ (for each surface triangle j) with a unit vector $\hat{n}_z$ along the z-axis (shown in Figure 1). The average surface orientation is obtained over all M triangles, and is presented as a distribution over the entire trajectory as:

$$\overline{\theta}_s = \frac{1}{M}\sum_{j=1}^{M}\hat{n}_s(j)\cdot\hat{n}_z. \quad (8)$$

Surface Time Correlation Functions. To examine the timescale of surface fluctuations time correlation functions were constructed for both $\delta\overline{h}_i(z)$ in Eqn. 5 and $\overline{\kappa_C^2}$ in Eqn. 7 using the generalized time correlation function for an observable X

$$C_X(t) = \langle X(0)\,X(t)\rangle. \quad (9)$$

Concentration Dependence of Surface Properties. Much prior work has been dedicated to understanding the macroscopic surface characteristics of water/vapor interfaces, including, but not limited to, surface tension and width as a function of different surfactant characteristics and concentration.[39–42] Extensive studies have further examined the orientation of polar solvents at the liquid/vapor interface through use of surface sensitive spectroscopies, as well as solute concentration gradients and organization at the surface.[43–46] Yet, connecting the surfactant adsorption to the geometry of the interface and its fluctuations is relatively unexplored. The geometric properties of the surface are of growing importance

n(TBP)	Surface coverage of TBP $(n/\text{Å}^2)$	d (Å)	γ(mN/m)	$\langle \Delta A \rangle_t$ (Å^2)	ΔG_{def}(kJ/mol)
0	0	1.82	47.80 ± 0.14	52.37	25.03
48	0.0064	2.21	46.91 ± 0.18	258.61	121.31
96	0.0126	2.41	44.30 ± 0.25	423.88	187.78
144	0.0184	3.62	39.57 ± 0.44	632.06	250.11
192	0.0242	4.43	38.28 ± 1.12	740.09	295.52
240	0.0291	4.68	36.03 ± 0.61	1059.86	381.87

Chain length n$_C$	Surface coverage $(n/\text{Å}^2)$	d (Å)	γ(mN/m)	$\langle \Delta A \rangle_t$ (Å^2)	ΔG_{def}(kJ/mol)
1 (TMP) $n = 96$	0.0032	2.01	45.77 ± 0.48	3851.23	1762.70
2 (TEP) $n = 96$	0.0054	2.45	41.45 ± 0.21	4501.94	1866.05
3 (TPP) $n = 96$	0.0098	2.87	34.38 ± 0.11	1876.04	644.98

TABLE I: (Top) Surface coverage of TBP, interfacial width d, surface tension γ, the change in surface area ΔA and free energy of surface deformation ΔG_{def} as a function of TBP coverage at the water/vapor surface. (Bottom) Behavior of alkyl phosphates with different C-chain lengths (TMP = trimethyl phosphate, TEP = triethyl phosphate, TPP = tripropyl phosphate, TBP = tributyl phosphate).
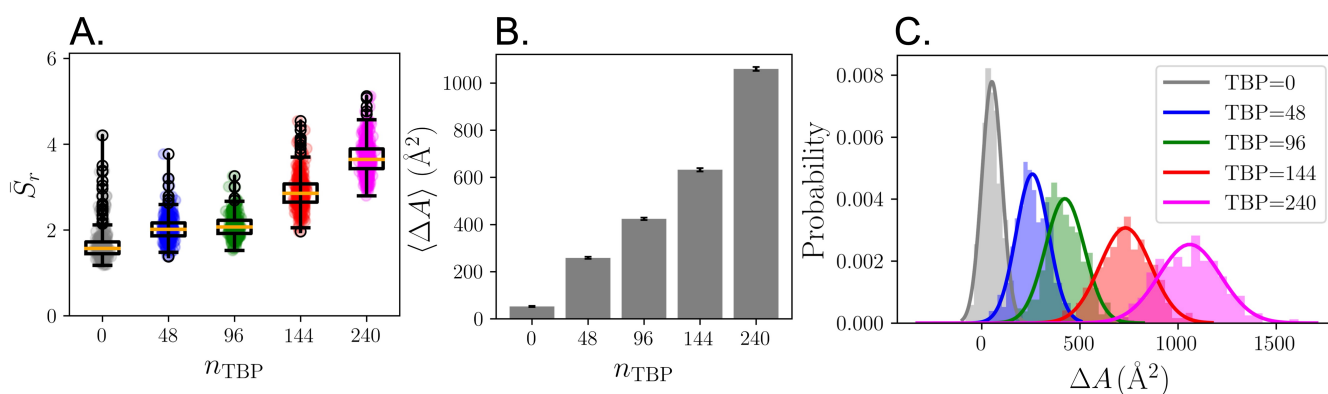

FIG. 2: (A.) Surface roughness ($\overline{S}_r$) as a function of n_{TBP} at water/vapor surface. The orange line in the boxplot signifies the median value, while the boundaries denote the 25th and 75th percentiles. (B.) Mean instantaneous water/vapor surface area and the respective standard deviations (plotted as error bars and obtained using the equation $\sigma/\sqrt{n}$, where σ is obtained from fitted Gaussian distribution functions). (C.) Distributions of ΔA for varying numbers of adsorbed TBP. An illustration of the gaussian fitting of ΔA is provided in the Figure S2.

because local surface organization creates microenvironments for reactivity.[47–50] We begin this study by examining geometric measures of the instantaneous surface and their associated temporal fluctuations as a function of TBP concentration.

As observed in Table I, the surface tension γ decreases from 47.80 ± 0.14 to 36.03 ± 0.61 mN/m as n_{TBP} increases from 0 to 240. Concurrently, there is an increase in interfacial width d and surface roughness $\overline{S}_r$ (Figure 2A). The increase in $\overline{S}_r$ and d indicate enhancement of the surface fluctuation, and the pronounced change in ΔA leads to a significant increase in the free energy of surface deformation with increasing TBP, from 25.03 kJ/mol in the pure vapor interface to 381.87 kJ/mol at

$n_{TBP} = 240$. As shown in Figure 2B, the average change to surface area increases in a linear fashion with TBP surface coverage, however this belies a significant change to the distribution of surface areas observed within the simulation trajectory. The ensemble distribution systematically becomes more broad (Figure 2C), where the full width of half maximum (FWHM) of the fitted Gaussians increase $\sim3\times$ from the pure water/vapor interface to the highest TBP surface coverage; this indicates large variations in the spatial fluctuations of the instantaneous surface.

Increases to spatial capillary wave fluctuations may occur homogeneously or inhomogeneously depending upon the competition of surfactant-surfactant vs. surfactant-
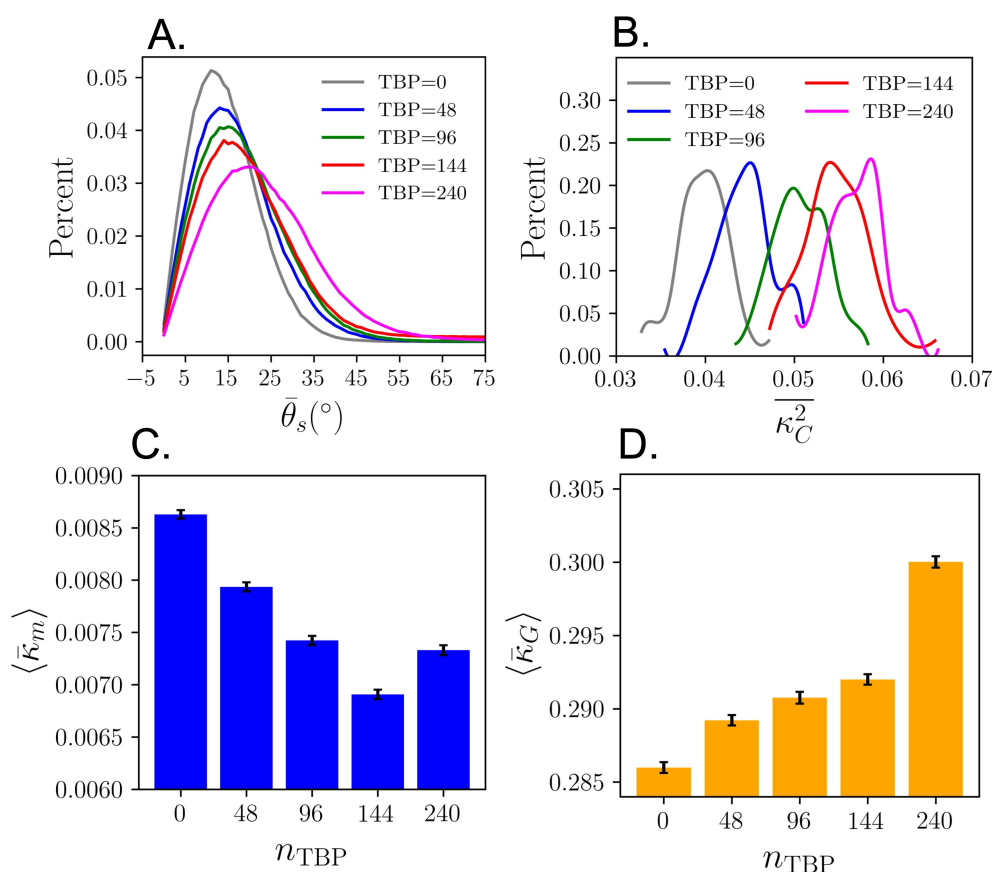
FIG. 3: (A.) The distributions of the surface normals orientation with increased TBP at water/vapor surface. (B.) The distribution of surface curvedness as a function of TBP adsorbed at the water/vapor surface. (C.) Mean curvature and (D.) Gaussian curvature as a function of the number of adsorbed TBP at water/vapor interface. The bar indicates the average calculated at each individual point on the surface, while the bracket signifies the average taken across all snapshots.

surface interactions. For example, there may exist areas of high curvature and areas of low curvature if the TBP does not form a homogeneous monolayer. In liquid/liquid systems, prior simulations have indicated TBP self-assembly at the interface, potentially forming larger macrostructures that are responsible for solute transport.[7] The structural origins behind the general changes to the surface structure that are defined by γ, d, $\overline{S}_r$, and ΔA are now analyzed by studying the average and ensemble distributions of different geometric measures.

We first examine the average surface orientation, which increases linearly ($R^2 = 0.97$) with the addition of TBP at the water/vapor surface (Figure S3). Study of the surface orientation $\overline{\theta}_s$ probability distributions (Figure 3A) shows that the peak maximum systematically increases with little change to the width of the distribution until a concentration of 240 TBP at which point there is a significant broadening and the formation of a shoulder in the distribution. Complementing this information

is the measure curvedness $\overline{\kappa_C^2}$ (Eqn.7), which describes the true curvature of the surface, irrespective of its sign corresponding to surface concavity or convexity. Higher values of curvedness represent more sharp (less broad) capillary wave features. The distributions of $\overline{\kappa_C^2}$ are presented in Figure 3B (average values presented in Figure S4) and show a systematic increase in surface curvature with increasing TBP.

Interestingly, a comparison of the mean ($\overline{\kappa}_m$) and Gaussian ($\overline{\kappa}_G$) curvatures reveals a transition in the affect of the surfactant upon the distribution of the surface wave geometries (Figure 3C-D). A linear decrease in $\overline{\kappa}_m$ is observed from the pure water/vapor interface until $n_{TBP} = 144$ is reached. At the same time, a slow but steady increase in $\overline{\kappa}_G$ is observed. The increase in $\overline{\kappa}_G$ reflects an increase one or both of the principle curvatures (curvature sharpness) of the surface (both being of the same sign). Yet the decrease in $\overline{\kappa}_m$ indicates that the convex and concave surface portions of the wave become better at cancelling one another as TBP concen-
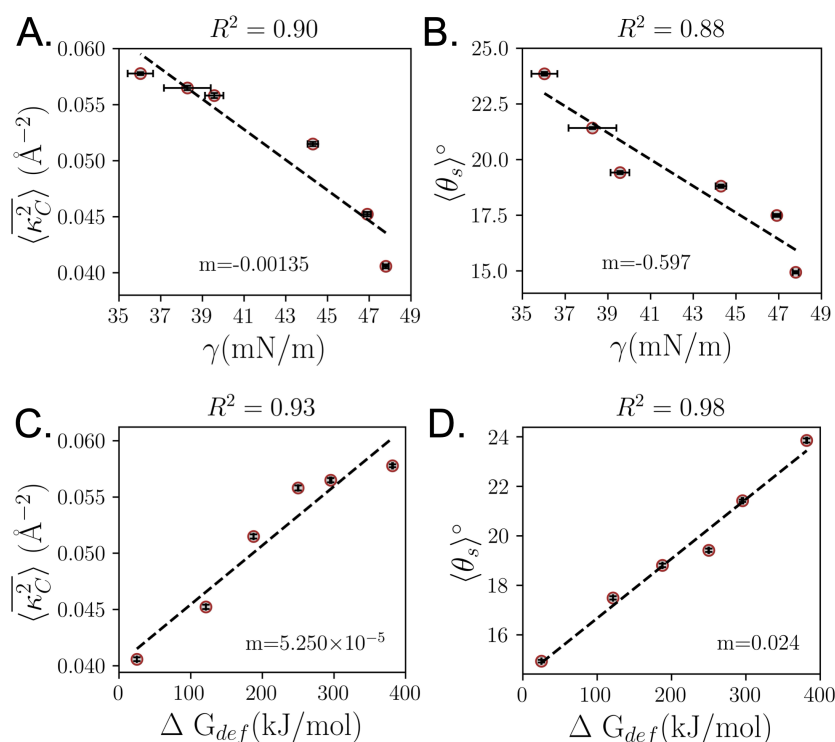
FIG. 4: Relationships of surface geometric descriptors with surface tension γ and deformation ΔG_{def} as a function of TBP surface coverage and fitted to a linear regression model with m being the slope: (A) time-averaged surface curvedness $\langle \overline{\kappa_C^2} \rangle$ vs. γ; (B) average surface orientation angle $\langle \overline{\theta}_s \rangle$ vs. γ; (C) $\langle \overline{\kappa_C^2} \rangle$ vs. ΔG_{def}; (D) $\langle \overline{\theta}_s \rangle$ vs. ΔG_{def}.

tration is increased. Thus, as TBP concentration is increased the surface waves become more pronounced but they do so in a *homogenous* fashion. At $n_{TBP} > 144$ an increase in $\overline{\kappa}_m$ is observed along with a significant increase in $\overline{\kappa}_G$. This indicates that the convex portions of the surface waves become much more pronounced and no longer cancel the concave portions. Such behavior we label as an *inhomogenous* change to the surface wave structure. This is consistent with the transition from a surface coverage where there were few TBP-TBP interactions to the coverage concentration that allows the formation of dimeric assemblies of TBP(H$_2$O)TBP on the surface that disrupt surface water hydrogen bonding and in liquid/liquid interfaces have been shown to be the basis of surface protrusions.[7]

To understand the impact of surfactant adsorption on the dynamics of surface fluctuations, time correlation functions of $\overline{h}_i(z)$ and $\overline{\kappa_C^2}$ are computed using Eqn. 9. It is observed that both $\overline{h}_i(z)$ and $\overline{\kappa_C^2}$ relaxes to 10% of its initial value within 0.01 ns in the pure liquid interface compared to 1 ns in the TBP = 240 system (Figure S5). The increase in TBP concentration delays the relaxation of the surface fluctuations which slows the time it takes for the surface waves to decorrelate; thus an inverse correlation is observed between surface relaxation

and surface tension in accordance with the capillary wave theory.[51, 52] At low TBP surface coverages, the time is nearly identical for curvedness and height as would be expected from capillary waves. However at the highest TBP concentration there is a further slow down in the relaxation of curvedness relative to height, as might be expected when TBP-TBP interactions dominate and become local self assembly amplifies surface curvature. In combination, the change in structural and temporal dynamics as a function of TBP surface coverage indicate a homogenous $\longrightarrow$ inhomogeneous transition in surface wave properties.

Relationships Between Surface Geometry and Macroscopic Properties. We next compare surface geometric descriptors against macroscopic surface properties for the TBP system as a function of surface coverage. As one might expect, surface curvedness $\langle \overline{\kappa_C^2} \rangle$ and the average orientation angle $\langle \overline{\theta}_s \rangle$ are anticorrelated with surface tension γ (higher surface tensions have low curvedness and surface orientation of the triangulated mesh). Yet the two measures of surface curvature have dramatically different sensitivities, with $\langle \overline{\theta}_s \rangle$ being nearly two orders of magnitude more sensitive with a similar quality of linear fit. Since γ is inversely related to surface deformation ΔG_{def}, surface curvedness and orientation are linearly

correlated with with this observable. In this case, both $\langle \overline{\theta}_s \rangle$ and $\langle \overline{\kappa_C^2} \rangle$ have a better quality of fit (higher R^2) than with γ, but again orientation is more sensitive than curvedness. The strong linear correlations is important in analytic model development, similar to that demonstrated by Ladanyi et al. for the surface fluctuations at pure liquid/liquid interfaces.[18]
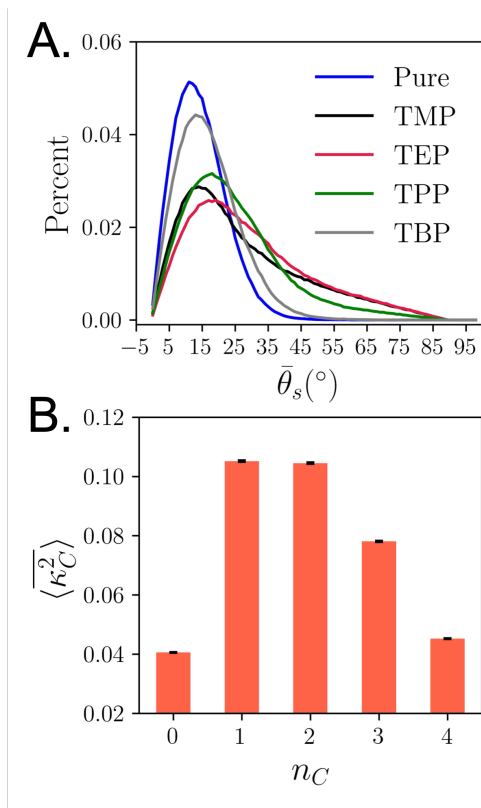

FIG. 5: Surface geometric metrics for trialkyl phosphates adsorbed at water/vapor surface with surface coverages between 3.2 - 9.8×10^{-2} $n/\text{Å}^2$ where "Pure" is the surface with no adsorbates, corresponding to an alkyl tail length carbon number n_C of zero. (A) The distributions of the surface orientation angles. (B) The average mean surface curvedness.

Role of Surfactant Tail Length. The alkyl tail chain length of alkyl phosphates dramatically impacts the associated water solubility (TBP ∼0.28-0.4 g/L, TPP 6.951 g/L and TEP 15.9 g/L).[53–55] As shown in Table I, the TMP, TEP, and TPP systems with 96 surfactants have surface coverage values that span 0.0032 - 0.0098 $n\text{Å}^{-2}$ are most similar to the TBP concentration with 48 TBP's per interface and having a coverage of 0.0064 $n\text{Å}^{-2}$. In this case, the surface tension values decrease in the order TMP > TPP > TEP, however the surface tension of TBP at this surface coverage is nearly that of TMP. Although the discrepency for TBP may be due to the specific force field employed, it is important to note that

the trend in surface deformation consistently decreases as the alkyl chain length is increased.

Interestingly, prior work has noted that in the case of TBP the surfactant adopts an interfacial orientation with the tails splayed on the surface akin to an umbrella and having the P=O group pointed toward the bulk water phase.[56] One might then anticipate that alkyl groups laying parallel to the surface might have a stabilizing or dampening affect upon the surface waves. This could potentially counteract the amplification of capillary wave curvature that occurs due to disruption of the interfacial hydrogen bond network of water that decreases surface tension and increases surface deformations. Indeed, this is observed in the highly right-skewed distribution of surface orientations $\overline{\theta}_s$ shown in Figure 5A, where the most observed orientation angle is $\approx 24°$ in TMP. As the akyl chain length is increased, the skewedness diminishes and the most probable orientation decreases to near 15 °. Concomittantly the total magnitude of curvedness, $\langle \overline{\kappa_C^2} \rangle$, shows a decrease as alkyl chain length is increased at these surface concentrations (prior to surfactant-surfactant interactions as indicated in the discussion above). These data indicate that smaller surfactants at low surface coverage can significantly enhance surface curvature and do so *inhomogenously*, whereas increasing the alkyl tail length induces a transition to a more homogeneous distribution of surface geometric properties. We label this an inhomogenous → homogeneous transition as a function of alkyl tail length of the surfactant.

In summary, this work explores the impact of adsorbed surfactants upon the geometric metrics of the liquid/vapor interface; comparing and contrasting the ensemble average versus distributions of these metrics indicates that there are regimes of transition between homogeneous changes to surface geometry (where the convex regions are reasonably symmetric with the concave regions) and inhomogeneous changes as a function of surface coverage or alkyl tail chain length. In the case of increasing surface coverage by TBP, homogeneous amplification of surface waves is observed until a concentration that supports TBP-TBP interactions which then induce inhomogenenous surface geometry distributions. Small alkyl phosphate surfactants with low surface coverage are observed to inhomogeneously amplify surface wave geometric properties; importantly, as the chain length is increased the alkyl tails cause more uniformity in the surface geometric metrics.

[1] O. Bjorneholm, M. H. Hansen, A. Hodgson, L.-M. Liu, D. T. Limmer, A. Michaelides, P. Pedevilla, J. Rossmeisl, H. Shen, G. Tocci, et al., Chemical Reviews **116**, 7698 (2016).

[2] R. Kusaka, S. Nihonyanagi, and T. Tahara, Nature Chemistry **13**, 306 (2021).

[3] B. Ocko, X. Wu, E. Sirota, S. Sinha, and M. Deutsch, Physical Review Letters **72**, 242 (1994).

[4] D. Schwartz, M. Schlossman, E. Kawamoto, G. Kellogg, P. S. Pershan, and B. Ocko, Physical Review A **41**, 5687 (1990).

[5] A. E. Ismail, G. S. Grest, and M. J. Stevens, The Journal of Chemical Physics **125** (2006).

[6] T. Zhou, A. McCue, Y. Ghadar, I. Bakó, and A. E. Clark, The Journal of Physical Chemistry B **121**, 9052 (2017).

[7] M. J. Servis and A. E. Clark, Physical Chemistry Chemical Physics **21**, 2866 (2019).

[8] N. Kumar and A. E. Clark, Chemical Science **12**, 13930 (2021).

[9] M. L. Schlossman and A. M. Tikhonov, Annu. Rev. Phys. Chem. **59**, 153 (2008).

[10] A. Pohorille and I. Benjamin, The Journal of Physical Chemistry **97**, 2664 (1993).

[11] H. W. Huang, Biophysical Journal **50**, 1061 (1986).

[12] V. Venkateshwaran, S. Vembanur, and S. Garde, Proceedings of the National Academy of Sciences **111**, 8729 (2014).

[13] F. P. Buff, R. A. Lovett, and F. H. Stillinger, Phys. Rev. Lett. **15**, 621 (1965).

[14] J. Chowdhary and B. M. Ladanyi, Phys. Rev. E **77**, 031609 (2008).

[15] P. Morgado, O. Lobanova, E. A. Müller, G. Jackson, M. Almeida, and E. J. Filipe, Molecular Physics **114**, 2597 (2016).

[16] G. M. Silva, P. Morgado, P. Lourenço, M. Goldmann, and E. J. Filipe, Proceedings of the National Academy of Sciences **116**, 14868 (2019).

[17] B. Smit, A. G. Schlijper, L. A. M. Rupert, and N. M. Van Os, The Journal of Physical Chemistry **94**, 6933 (1990).

[18] J. Chowdhary and B. M. Ladanyi, Physical Review E **77**, 031609 (2008).

[19] C. Fradin, A. Braslau, D. Luzet, D. Smilgies, M. Alba, N. Boudet, K. Mecke, and J. Daillant, Nature **403**, 871 (2000).

[20] J. Stecki, The Journal of Chemical Physics **109**, 5002 (1998).

[21] L. G. MacDowell, Phys. Rev. E **96**, 022801 (2017).

[22] J. Hernández-Muñoz, P. Tarazona, and E. Chacón, The Journal of Chemical Physics **157**, 154703 (2022), ISSN 0021-9606.

[23] L. Martínez, R. Andrade, E. G. Birgin, and J. M. Martínez, Journal of Computational Chemistry **30**, 2157 (2009).

[24] M. J. Abraham, T. Murtola, R. Schulz, S. Páll, J. C. Smith, B. Hess, and E. Lindahl, SoftwareX **1**, 19 (2015).

[25] D. J. Evans and B. L. Holian, The Journal of Chemical Physics **83**, 4069 (1985).

[26] B. Hess, H. Bekker, H. J. Berendsen, and J. G. Fraaije, Journal of Computational Chemistry **18**, 1463 (1997).

[27] E. Neria, S. Fischer, and M. Karplus, The Journal of Chemical Physics **105**, 1902 (1996).

[28] X. Ye, S. Cui, V. F. de Almeida, and B. Khomami, The Journal of Physical Chemistry B **117**, 14835 (2013).

[29] J. Wang, R. M. Wolf, J. W. Caldwell, P. A. Kollman, and D. A. Case, Journal of Computational Chemistry **25**, 1157 (2004).

[30] A. P. Willard and D. Chandler, The Journal of Physical Chemistry B **114**, 1954 (2010).

[31] Z. Liu, T. Stecher, H. Oberhofer, K. Reuter, and C. Scheurer, Molecular Physics **116**, 3409 (2018).

[32] W. E. Lorensen and H. E. Cline, ACM Siggraph Computer Graphics **21**, 163 (1987).

[33] M. Sega, G. Hantal, B. Fábián, and P. Jedlovszky (2018).

[34] J. Alejandre, D. J. Tildesley, and G. A. Chapela, The Journal of Chemical Physics **102**, 4574 (1995).

[35] I. Benjamin, Ann. Rev. Phys. Chem. **48**, 407 (1997).

[36] B. Suhr, W. A. Skipper, R. Lewis, and K. Six, Scientific Reports **10**, 1 (2020).

[37] J. J. Koenderink and A. J. Van Doorn, Image and Vision Computing **10**, 557 (1992).

[38] S. Z. Li, Computer-Aided Design **27**, 235 (1995).

[39] H. S. Alasiri, A. S. Sultan, and W. G. Chapman, Energy & Fuels **33**, 6678 (2019).

[40] C. Vega and E. de Miguel, The Journal of chemical physics **126** (2007).

[41] M. Peng, T. T. Duignan, C. V. Nguyen, and A. V. Nguyen, Langmuir **37**, 2237 (2021).

[42] H. B. de Aguiar, A. G. de Beer, M. L. Strader, and S. Roke, Journal of the American Chemical Society **132**, 2122 (2010).

[43] S. Nihonyanagi, J. A. Mondal, S. Yamaguchi, and T. Tahara, Annual Review of Physical Chemistry **64**, 579 (2013).

[44] H. C. Allen, D. Gragson, and G. Richmond, The Journal of Physical Chemistry B **103**, 660 (1999).

[45] N. Kumar, M. J. Servis, and A. E. Clark, Solvent Extraction and Ion Exchange **40**, 165 (2022).

[46] B. Doughty, P. Yin, and Y.-Z. Ma, Langmuir **32**, 8116 (2016).

[47] E. Alvarado, Z. Liu, M. J. Servis, B. Krishnamoorthy, and A. E. Clark, Journal of Chemical Theory and Computation **16**, 4579 (2020).

[48] N. Kumar and A. E. Clark, Journal of Chemical Theory and Computation **19**, 3303 (2023).

[49] N. Zarayeneh, N. Kumar, A. Kalyanaraman, and A. E. Clark, Journal of Chemical Theory and Computation **18**, 7043 (2022).

[50] S. W. Devlin, I. Benjamin, and R. J. Saykally, Proceedings of the National Academy of Sciences **119**,

e2210857119 (2022).

[51] A. K. Thakre, J. Padding, W. K. den Otter, and W. J. Briels, The Journal of chemical physics **129**, 044701 (2008).

[52] S. P. Niblett and D. T. Limmer, The Journal of Physical Chemistry B **125**, 2174 (2021).

[53] P. Velavendan, S. Ganesh, N. Pandey, R. Geetha, M. Ahmed, U. Kamachi Mudali, and R. Natarajan, Journal of Radioanalytical and Nuclear Chemistry **295**, 1113

(2013).

[54] C. Higgins, W. Baldwin, and B. Soldano, The Journal of Physical Chemistry **63**, 113 (1959).

[55] W. Apostoluk and W. Robak, SN Applied Sciences **1**, 801 (2019).

[56] Y. Ghadar and A. E. Clark, Phys. Chem. Chem. Phys. **16**, 12475 (2014).